A Pareto-Optimal Characterization of Miniaturized Distributed Occulter/Telescope Systems

Adam W. Koenig[a], Simone D'Amico[a], Bruce Macintosh[b], and Charles J. Titus[b]

[a]Stanford University, Department of Aeronautics and Astronautics, Space Rendezvous Laboratory, Durand Building, 496 Lomita Mall, Stanford, CA 94305, United States;
[b]Stanford University, Department of Physics, 382 Via Pueblo Mall, Stanford, CA 94305, United States

ABSTRACT

Distributed occulter/telescope systems hold great promise in the field of direct exoplanet imaging. However, proposed missions using this concept such as the New Worlds Observer or Exo-S (NASA) are exceptionally large with occulter diameters of tens of meters and inter-spacecraft separations of tens of megameters, requiring deployment in deep space. The estimated costs associated with these missions are in the billions of dollars. In order to reduce the risk associated with these missions, it is desirable to first deploy a low-cost technology demonstrator mission to prove that the distributed occulter telescope concept is valid. To that end, this work assesses the feasibility of miniaturizing the optics of the distributed occulter/telescope to enable deployment on micro- or nano-satellites in earth orbit. A variant of the convex optimization formulation introduced by previous authors is used to generate a pareto-optimal characterization between the achievable occulter contrast and a set of critical design variables (occulter radius, inner working angle, science spectrum, etc). This characterization is performed for two different sets of engineering constraints, corresponding to different levels of design complexity. The results of this study are compared to the performance requirements for imaging targets of scientific interest, namely exozodiacal dust disks, in order to identify promising design envelopes. The result of this work is a comprehensive trade of the capabilities of miniaturized, binary, petal-shaped occulters. This research demonstrates that there exist miniaturized occulter geometries compatible with micro- or nano-satellites in earth orbit suitable for imaging exozodiacal dust disks. In addition, this study provides a valuable methodology and performance guidelines for future distributed occulter/telescope designs.

Keywords: Exoplanets, starshades, occulters, miniaturization

1. INTRODUCTION

The detection and characterization of extrasolar planets, or exoplanets, is a topic of great interest to the scientific community. To date, indirect detection methods such as transit photometry, gravitational microlensing, and radial velocity methods have been used for most confirmed detections. Specifically, NASA's Kepler mission is responsible for over 1000 exoplanet discoveries.[1] However, indirect methods provide little information beyond the planet's mass, size, orbit period, and orbit radius. Direct imaging would instead allow scientists to study the chemical composition of exoplanets. Data gathered from direct imaging instruments could enable identification of key biosignature gases such as water, oxygen, and carbon dioxide. However, direct imaging of exoplanets is challenging problem from an optics standpoint due to their small angular separations and low brightness. For example, an Earth-like planet orbiting a star 10 parsecs away will have an angular separation of 100 milliarcseconds (mas) and is approximately 10^{-10} as bright as its parent star. There are two primary methods of directly imaging exoplanets: 1) telescopes with internal coronagraphs and adaptive optics and 2) distributed systems consisting of an occulter spacecraft and a telescope spacecraft. Although internal coronagraphs have met with

Further author information: (Send correspondence to A.W.K.)
A.W.K.: E-mail: awkoenig@stanford.edu
S.D.: E-mail: damicos@stanford.edu, Telephone: 650 497 4682
B.M.: E-mail: bmacintosh@stanford.edu, Telephone: 650 725 4116
C.J.T.: E-mail: ctitus@stanford.edu

some success[2] and are being considered for spaceborne observatories (NASA Exo-C[3] and WFIRST-AFTA[4]), they are both expensive and complex.[5] Recent advances in formation flying technologies[6–8] suggest that it is possible to use an occulter on a separate spacecraft to attenuate the light from a star, negating the need for complex internal optics in the telescope. Indeed, several missions including Exo-S (NASA)[9] and the New Worlds Observer (NWO) (NASA)[5] have been proposed to image earth-like planets using visible wavelengths. These missions call for occulters tens of meters in diameter and inter-spacecraft separation distances of tens of megameters. On account of the large separation requirement, these missions cannot be implemented in earth orbit and are instead proposed to be deployed at Lagrange points. Because of these demanding requirements, these missions have predicted costs in the billions of dollars.

In order to reduce the risk associated with such an expensive mission, it is desirable to first deploy a miniaturized technology demonstrator. Such a mission would demonstrate the validity of the distributed occulter/telescope concept, develop some of the critical enabling technologies for large-scale missions, and collect images of a small set of scientifically relevant targets, namely exozodiacal dust disks or bright exoplanets. To that end, we have begun investigations of a miniaturized distributed occulter/telescope (mDOT) mission concept consisting of an occulter and telescope deployed on separate micro- or nano-satellites in earth orbit.[10] Using small satellites in earth orbit introduces a number of challenges. First, formations in earth orbit are subjected to larger differential accelerations than formations depoyed at Lagrange points. Second, using a small occulter will require centimeter-level relative navigation precision during observations. Third, small satellites have limited on-board resources and low technology readiness level for precision guidance, navigation, and control (GN&C) systems. Finally, shrinking the occulter to a size compatible with micro- or nano-satellites has significant consequences on the achievable contrast. Occulter design studies in literature have focused primarily on detection of earth-like planets in the visible spectrum. These studies can be broadly divided into two approaches: 1) analytical formulations based on offset hypergaussian functions,[5] and 2) numerical methods based on convex optimization.[11] Previous authors have studied the effects of scaling down the occulter,[12,13] but these studies focus exclusively on imaging exoplanets and fail to account for all relevant design considerations. Furthermore, there are couplings between aspects of the optical system and the formation design problem in earth orbit that are not discussed in literature. In light of these limits, the objective of this paper is to present a comprehensive study of binary, petal-shaped occulters suitable for deployment on micro- or nano-satellites in earth orbit. The primary contribution of this paper is a pareto-optimal characterization of the achievable contrast of these occulters across all critical design variables. These results are used to identify promising regions in the design space for imaging a variety of scientifically interesting targets, namely exozodiacal dust disks or exoplanets. This paper also includes an analysis of the relationship between manufacturing considerations and occulter contrast performance.

2. SCIENCE TARGET MODELING

Although the science case for full-scale occulter missions is driven by imaging extrasolar planets, this is not practical for very small-scale missions. An external occulter can overcome the challenging contrast levels, in the ideal case, almost perfectly blocking out the parent star for planets outside the inner working angle. However, a second obstacle remains. Planets are intrinsically very faint. A jupiter analog orbiting even the nearest stars has a visual magnitude of 23 or fainter. This corresponds to a flux of 0.001 photons per second per centimeter squared.

This signal is extremely difficult to detect with small telescopes. Even if the occulter perfectly blocks the host star, detector noise and Poisson noise from the background zodiacal light in our solar system and possibly the zodiacal analog in the target system can swamp the planetary signal. Figure 1 shows the exposure time needed for a 5-sigma detection of a hypothetical planet orbiting the bright star Vega at 3.5 AU (corresponding to a 500 mas inner working angle), given the parameters in Table 1 for a range of telescope diameters. These exposure times are clearly impractical. There are some stellar targets that are slightly more favorable (e.g. Alpha Centauri), but these generally have other complications (e.g. Alpha Centauri is a binary star and there is no Doppler evidence for a Jovian planet present). Statistics from existing Doppler surveys indicate that Jupiter-sized planets are rare with $\sim$2% of stars having a giant planet between 0.3 and 3 AU,[14] so a survey that targets a few stars will likely not discover anything. The one possible exception is the giant planet tentatively detected by Doppler shifts orbiting the star Epsilon Eridani.[15] However, because Epsilon Eridani is a fainter, redder star,

exposure times would be approximately 12 times longer than those in Figure 1. Exoplanet detection remains an interesting science driver for medium-sized telescopes but impractical for small telescopes.

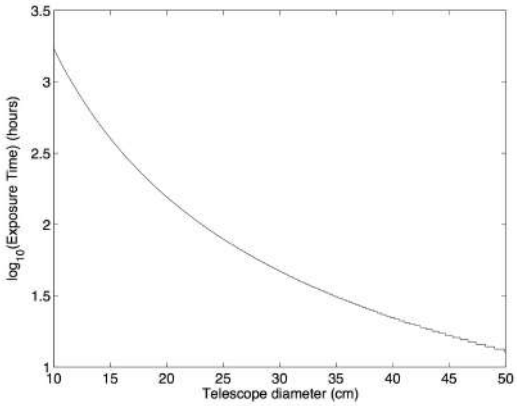

Figure 1. Necessary exposure time for 5-sigma detection of hypothetical planet orbiting Vega at 3.5 AU vs aperture diameter

Table 1. Fiducial telescope model

Bandpass	200-300 nm
Throughput of camera	79%
QE of detector	80%
Read noise	3 e^-/pixel
Dark current	0.0016 e^-/(pixel sec)

However, a small telescope has significant sensitivity to extrasolar dust disks - zodiacal light and debris disks. As seen from outside our solar system, the integrated light from zodiacal dust is actually a hundred times brighter than Jupiter - $F_{disk}/F_{sun} = 10^{-7}$. Similar disks have been detected around many nearby stars through thermal emission, which is detectable as excess infrared flux compared to the predicted stellar spectrum (the Vega phenomenon). These detections show that for many stars the total mass of dust is much higher than in our solar system, with F_{disk}/F_{star} as high as 10^{-3}. In most cases, the dust disk has been detected only through thermal emission at long wavelengths. Visible or near-infrared scattered light has been seen in some favorable cases (e.g. Beta Pictoris) with coronagraphy, but not many. Detecting the scattered light from disks that have only been seen in the infrared, especially low total brightness disks, would be scientifically extremely interesting. Comparison of ultraviolet to visible to infrared brightness would help constrain the size of the scattering particles and polarization properties could even provide information about their shape (e.g. Graham et al.[16]). Detecting these disks is therefore both practical and scientifically compelling.

Figure 2 shows the required exposure time to detect a disk with the same geometry as that orbiting Beta Pictoris with a 10-cm telescope as a function of F_{disk}/F_{star} using an occulter with a contrast between 10^{-5} and 10^{-9}. However, several important caveats must be added. The detectability of the disk will depend not only on its total emission, but also on its geometry. An edge-on disk like Beta Pictoris is favorable since the light of the (optically thin) disk is concentrated over a small region of the science field of view and morphologically distinct from most scattered light artifacts. An extended face-on disk occupies more detector pixels, reducing sensitivity, and may resemble the broad halo of light leaking through an occulter or internal coronagraph. Finally, the plot in Figure 2 shows only the time required to detect the total disk photometrically by summing all the light over the disk's extent. Resolving structure in the disk would require significantly longer. For example, to obtain an image with the disk detected in N distinct regions increases the exposure time by roughly N. Still, these calculations show that even moderately bright disks ($F_{disk}/F_{star} > 10^{-6}$) will be detectable. Brighter disks may

be partially resolved, allowing measurement of inclination and brightness vs azimuth. If the mission could detect $F_{disk}/F_{star} > 10^{-7}$ (e.g. with a larger telescope and perhaps PSF subtraction techniques) with an inner working angle of approximately 500 mas, it would satisfy the goal identified in the Decadal Survey[17] of characterizing zodiacal emission around nearby stars.

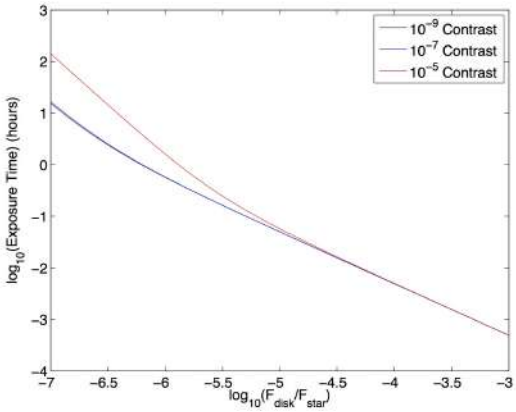

Figure 2. Necessary exposure time to disk exozodiacal disk with same geometry as Beta Pictoris for 10 cm telescope plotted against fractional brightness, F_{disk}/F_{star} for occulter contrast ranging from 10^{-9} to 10^{-5}

3. PROPOSED MISSION CONCEPT

We endeavor to design a mDOT mission that will demonstrate the feasibility of the distributed occulter/telescope mission concept by imaging a small set of targets of scientific interest, namely exozodiacal dust disks (though exoplanets are not in principle excluded). Before proceeding into the optical analysis, we first describe the envisioned mission concept. It is known that faint exozodii will require several hours of instrument integration time using a small telescope. Conducting such a long observation in one continuous pass in earth orbit is highly impractical. Indeed, as demonstrated by the authors,[18] appropriate formation design can substantially reduce the delta-v cost associated with formation keeping, thereby increasing the mission lifetime and available instrument integration time. In light of these results, the envisioned mission operations strategy divides nominal operations into two phases, similar to the European Space Agency's PROBA-3 solar coronagraph concept:[19] 1) a science phase during which a low-thust, continuous control system will keep the formation in alignment with decimeter precision while the telescope instrument images the target, and 2) a reconfiguration phase during which the formation is impulsively corrected to ensure alignment at the start of the next science phase. The proposed mission concept is subject to distinct challenges compared to PROBA-3 including inter-spacecraft separations of hundreds of kilometers and the resource limitations of small satellites. This operations concept is illustrated in Figure 3. In the figure it is assumed that the telescope spacecraft maintains alignment during the science phase and the occulter spacecraft performs the impulsive reconfiguration maneuvers, though these responsibilities can be delegated as necessary.

A key feature of the proposed concept is that the science phase control system only counteracts the differential acceleration perpendicular to the line-of-sight to minimize the delta-v cost associated with forced motion control. The authors have demonstrated that there exist formations where the differential acceleration perpendicular to the line-of-sight due to the spherical component of earth gravity is identically zero.[18] Performing finite observations near these configurations can reduce the time-average control cost of the science phase to the order of $\mathrm{mm\,s^{-2}}$. Using this strategy, the spacecraft freely drift along the line-of-sight during science operations. Thus, it is imperative that the occulter contrast be sufficient for science operations over a range of separation distances. The authors have found that the available observation time using this operations model depends on the ratio of the allowed drift to the baseline separation and the orbit radius of the formation when science observations are conducted. It has been found that allowing the spacecraft to drift by 1% of the baseline separation in either direction is sufficient to allow science observations of at least one hour per orbit, provided that the orbit radius is

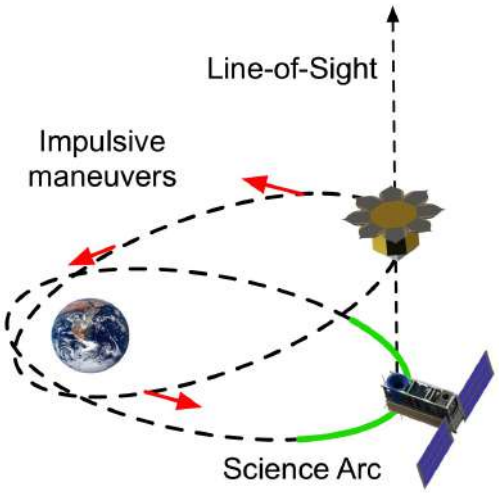

Figure 3. Illustration of telescope and occulter orbits (not to scale) noting quasi-continuous alignment control during the science phase (green) and impulsive control during the reconfiguration phase (red)

at least 30 000 km during observations. Additionally, the authors have found that the delta-v cost associated with mission operations is minimized when the formation is aligned with the angular momentum vector of the orbit of the telescope spacecraft during the science phase. For a more detailed explanation of the optimal formation design of distributed telescopes in earth orbit, the reader is referred to the orbit analysis concurrently published by the authors.[18]

4. DESIGN ENVELOPE

The design envelope for miniaturized occulters is developed from a simple set of considerations. These considerations include the geometric requirements of diffractive optics, mission operations requirements, and requirements to manufacture and deploy the occulter. For clarity, we divide the design envelope constraints into two sections: geometric considerations based on the required size of the occulter and shadow, and engineering constraints governing realizable occulter geometries.

4.1 Geometric Design Envelope

In order to define the design envelope from geometric considerations, consider the model illustrated in Figure 4. In this figure, R is the radius of the occulter, z is the baseline inter-spacecraft separation, Δz is the allowable drift from the baseline before shadow performance decays beyond tolerable levels, and ρ is the radius of the shadow sufficiently deep to allow scientific observations. In addition, ω is the inner working angle (IWA) of the occulter, f is the Fresnel number of the occulter, and λ denotes the wavelength of light being considered. The Fresnel number is equivalent to the path length difference between the center and edge of the occulter to the center of the telescope measured in half-wavelengths. It can be seen that not all of these variables are independent. Specifically, there are two constraints governing the relationship between R, z, ω, f, and λ. The constraint equation for ω is given by

$$\omega = \arctan \frac{R}{z} \approx \frac{R}{z} \tag{1}$$

and the constraint equation for the Fresnel number according to Goodman[20] is given by

$$f = \frac{R^2}{\lambda z}. \tag{2}$$

For clarity, plots of the relationships between R, z, ω, and f are included in Appendix A for wavelengths ranging from 150 to 600 nm. It can be seen that because the system has been scaled down by more than an order of

magnitude compared to large-scale missions, miniaturized occulters only begin to have reasonable Fresnel numbers in the ultraviolet spectrum. Thus, it would appear that using an ultraviolet telescope would allow complete recovery of optical performance. However, there are two challenges to this approach. First, conventional mirror performance sharply degrades for wavelengths below 150 nm. Second, most stars have a very small fraction of their luminous output in the ultraviolet spectrum. Thus, the ultraviolet flux from interesting targets will be very low, resulting in long integration times. Increasing the maximum wavelength of the science instrument will increase the available flux, but decrease the achievable occulter contrast. It is therefore clear that the ideal occulter for imaging a specified target depends on the emission spectrum of the target and the required contrast.

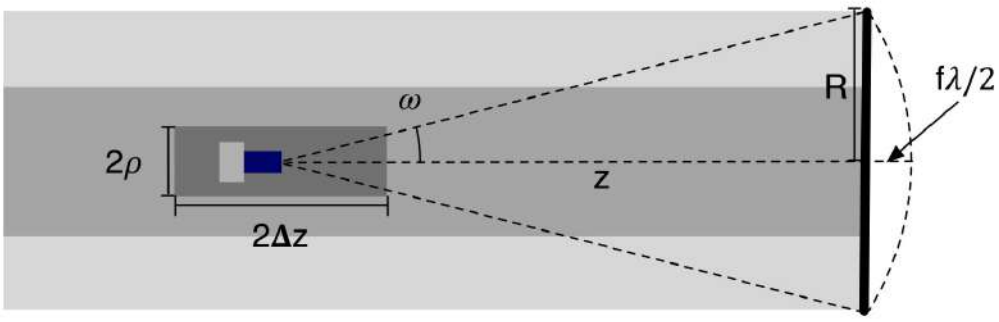

Figure 4. Configuration of occulter and telescope spacecraft

From these considerations we can develop a simple set of bounds on the size of the occulter, the size of the required shadow, the inter-spacecraft separation, and the science spectrum. First, consider the occulter size. It is estimated that the occulter radius can be as large as 1 m without requiring a complex deployment mechanism on a micro-satellite by folding the petals onto the sides of the spacecraft bus. In addition, since the occulter must be larger than the required shadow in order to achieve a useful contrast level, a reasonable lower bound for the occulter radius is 0.2 m. Next, consider the inter-spacecraft separation. In order to produce useful images of exozodiacal dust disks, the inner working angle should be no larger than 1000 mas. From Appendix A it is evident that occulters with inner working angles of less than 100 mas will not be able to achieve scientifically relevant contrast. An inner working angle range of 100 to 1000 mas corresponds to an inter-spacecraft separation range of 200 to 2000 km for a 1 m radius occulter. Now, consider the required shadow size. The shadow must be sufficiently large that the entire telescope aperture remains in the shadow of the occulter for the duration of the observation. Thus, the shadow radius must be no smaller than the sum of the radius of the telescope aperture and the precision of the formation GN&C system. A CubeSat can accommodate a telescope aperture diameter of up to 10 cm. To establish an upper bound on the shadow size, consider that the shadow size cannot reasonably exceed the size of the occulter. Indeed, previous design studies[5] suggest that the shadow radius is limited to a small fraction of the occulter radius. In order to comprehensively characterize the relationship between achievable contrast and shadow radius, this study allows for shadow radii as large as 60 cm. Next, consider the spectrum of the science instrument. As previously mentioned, conventional reflectors have poor performance for wavelengths below 150 nm. Furthermore, as shown in Appendix A, the Fresnel number is very low within the geometric envelope for wavelengths larger than 450 nm. Thus the spectrum of the science instrument is limited to 150 to 450 nm. In order to characterize the effect of the bandwidth of the science instrument, we allow bandwidths ranging from 25 nm to 200 nm within this spectrum. Finally, as mentioned in Section 3, for this analysis it is required that occulter performance does not degrade beyond tolerable levels if the inter-spacecraft separation varies by up to 1% of the baseline. In light of these considerations, the sampling of the design envelope used for this study is described in Table 2. The values in Table 2 were selected in order to include a uniform sampling of six independent design variables. Using the optimization formulation described in the following section, an optimal occulter geometry is generated or every possible combination of these six variables with a few exceptions. These occulter geometries are used to characterize the relationship between the achievable contrast and each of

the critical design variables.

Table 2. Miniaturized occulter design envelope

R (m)	z (km)	ρ (m)	λ_{max}(nm)	Bandwidth (nm)	R_{solid}/R
5 pts.	10 pts.	6 pts.	6 pts.	6 pts.	4 pts.
0.2	206	0.1	175	25	0.2
0.4	229	0.2	225	50	0.4
0.6	257	0.3	275	75	0.6
0.8	294	0.4	325	100	0.8
1.0	343	0.5	375	150	-
-	412	0.6	425	200	-
-	516	-	-	-	-
-	688	-	-	-	-
-	1031	-	-	-	-
-	2062	-	-	-	-

4.2 Engineering Design Envelope

The engineering design envelope includes necessary constraints on the occulter shape to ensure that the occulter is physically realizable and structurally sound. Additionally, in order to characterize the relationship between achievable contrast and occulter shape constraints, this study includes two distinct engineering models representing different manufacturing and deployment complexity levels. Following the convention of Vanderbei,[11] the occulter geometry is defined by an apodization function, $A(r)$, which denotes the fraction of the arc at radius r covered by the petal. The relationship between the apodization function and the resulting petal geometry is illustrated in Figure 5. In the figure, θ is the angle subtended by the petal and $A(r)\theta$ is the fraction of this angle

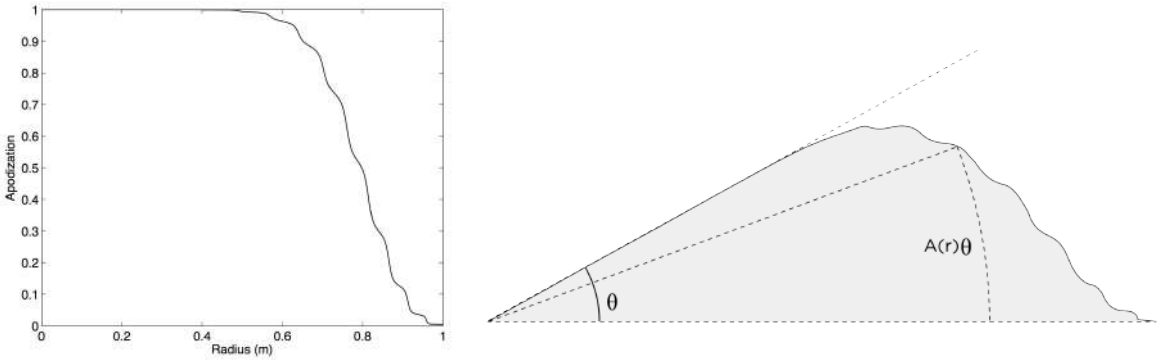

Figure 5. Illustration of relationship between apodization function and petal geometry with apodization function profile (left) and resulting petal geometry (right)

covered by the petal expressed as a function of the radius. In order to ensure realizable and structurally sound petal geometries, three constraints modeled after Vanderbei's[11] design problem are applied to both engineering models. First, the occulter geometry shall include a solid disk of radius R_{solid} to accommodate the spacecraft bus. Using the above description, this constraint is given by

$$A(r) = 1 \qquad r < R_{solid}. \tag{3}$$

Second, the occulter apodization function shall decrease monotonically in order to ensure structurally robust petal shapes. This constraint prevents designs requiring thin members to support large areas of the petal. This constraint is given by

$$\frac{dA}{dr}(r) \leq 0 \qquad 0 \leq r \leq R. \tag{4}$$

The third constraint specifies that the apodization function function must be sufficiently smooth to allow the geometry to be precisely manufactured. If it is assumed that the occulter is machined with a 1 mm diameter bit, it is necessary that the maximum curvature of the occulter geometry, c_{max}, be less than the curvature of the bit. The curvature of the occulter with a specified apodization profile depends on the number of petals, N. The curvature constraint can therefore be expressed as

$$\frac{\pi r}{N}\left|\frac{d^2A}{dr^2}(r)\right| \leq c_{max} \qquad 0 \leq r \leq R. \tag{5}$$

The following sections describe the unique geometric constraint associated with each engineering model.

Model 1: Minimum Complexity

The model includes occulters designed to minimize manufacturing and deployment complexity. To that end, it is required that the petals be shaped such that they can be folded onto the sides of the spacecraft bus without interference. This occulter design is illustrated with petals stowed and deployed in Figure 6. Designing the petals such that they can be folded onto the sides of the spacecraft bus imposes a geometric constraint, which is given by

$$A(r) \leq \frac{N}{\pi}\arcsin\left(\frac{R_{solid}\sin\left(\pi/N\right)}{r}\right) \qquad R_{solid} \leq r \leq R. \tag{6}$$

It can be seen that the upper bound of the apodization function depends on the number of petals. However, the difference in the upper bound for 4 petals and nearly infinite petals can be shown to be small. For this study the conservative constraint associated with 4 petals is enforced.

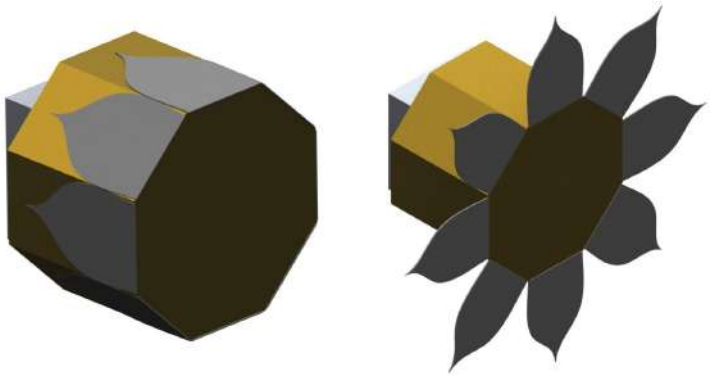

Figure 6. Model 1 petal deployment stages

Model 2: Compound Folded Petals

This model is intended to include occulters with improved contrast performance with only a modest increase in design complexity. Similar to the Model 1 occulters, this model assumes that the petals are initially stowed on the side of the spacecraft bus. However, this model allows for a 2-stage deployment system via winglets on the primary petals. After the primary petals deploy outward from the sides of the spacecraft bus, these winglets deploy outward from the primary petals. This model is illustrated in deployment stages in Figure 7. The geometric constraint for this model is very similar to the constraint applied to Model 1, but is less restrictive. This constraint is given by

$$A(r) \leq \frac{N}{\pi}\arcsin\left(\frac{2R_{solid}\sin\left(\pi/N\right)}{r}\right) \qquad 2R_{solid} \leq r \leq R. \tag{7}$$

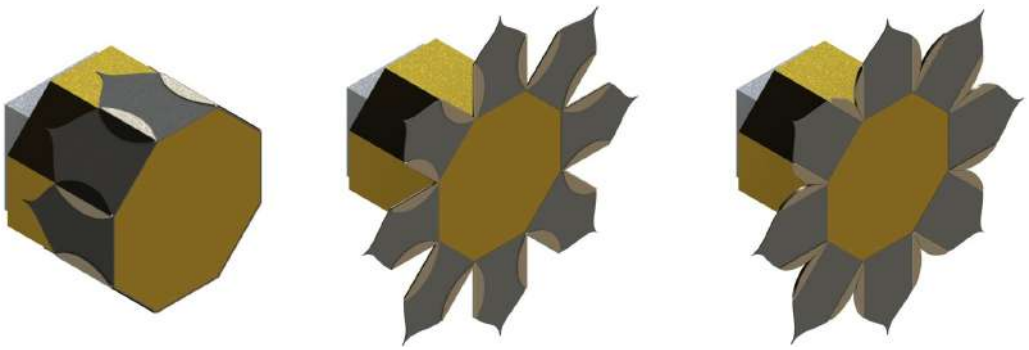

Figure 7. Model 2 petal deployment stages

It can be seen that this constraint has no impact on the occulter geometry if $R_{solid} \geq 0.5R$. For this analysis we again enforce the conservative constraint associated with 4 petals.

5. OPTIMIZATION PROBLEM FORMULATION

We endeavor to design a binary occulter that minimizes the scattered starlight over a specified spectrum in a specified spatial region. This is accomplished by numerically solving a variant of the convex optimization problem posed by Vanderbei,[11] which is briefly summarized below. Let the light from a star be modeled as a plane wave with complex scalar amplitude, E_0, and wavelength, λ. Additionally, let the electric field in the telescope aperture plane, E, be expressed as a function of polar coordinates including radius, ρ, and angle, ϕ. The electric field in the aperture plane is given according to the Jacobi-Anger expansion by

$$\begin{aligned} E(\rho,\phi;\lambda) = E_0\, e^{2\pi i z/\lambda}\Big(1 - \frac{2\pi}{i\lambda z}\int_0^R A(r)\, J_0\Big(\frac{2\pi\rho r}{\lambda z}\Big)\, e^{\frac{\pi i}{\lambda z}(r^2+\rho^2)} r\, dr\Big) \\ -E_0\, e^{2\pi i z/\lambda}\sum_{j=1}^{\infty}\frac{(-1)^j 2\pi}{i\lambda z}\Big(\int_0^R e^{\frac{\pi i}{\lambda z}(r^2+\rho^2)} J_{jN}\Big(\frac{2\pi\rho r}{\lambda z}\Big)\frac{sin(i\pi A(r))}{i\pi} r\, dr\Big) \\ \times(2\cos(jN(\phi-\pi/2))), \end{aligned} \tag{8}$$

where N is the number of petals, which is assumed to be even. For sufficiently large N, it has been shown that ϕ-dependent terms only play a role far from the optical axis. As such, the electric field in the aperture plane can reasonably be approximated by

$$E(\rho;\lambda) = E_0\, e^{2\pi i z/\lambda}\Big(1 - \frac{2\pi}{i\lambda z}\int_0^R A(r)\, J_0\Big(\frac{2\pi\rho r}{\lambda z}\Big)\, e^{\frac{\pi i}{\lambda z}(r^2+\rho^2)} r\, dr\Big). \tag{9}$$

Using this formulation of the electric field and considering the engineering requirements placed on the occulter geometry, the optimization problem is given by

$$\text{minimize } \gamma^2$$

$$\text{subject to:}$$

$$A(r) = 1 \qquad 0 \leq r \leq R_{solid}$$
$$\tfrac{dA}{dr} \leq 0 \qquad 0 \leq r \leq R$$
$$\tfrac{\pi r}{4}\left|\tfrac{d^2A}{dr^2}(r)\right| < 2000 \text{ m}^{-1} \qquad 0 \leq r \leq R$$
$$|\mathbb{R}(E(\rho,z;\lambda))| < \gamma/\sqrt{2} \qquad 0 \leq \rho \leq \rho_{max} \qquad z_{min} \leq z \leq z_{max} \qquad \lambda_{min} \leq \lambda \leq \lambda_{max}$$
$$|\mathbb{I}(E(\rho,z;\lambda))| < \gamma/\sqrt{2} \qquad 0 \leq \rho \leq \rho_{max} \qquad z_{min} \leq z \leq z_{max} \qquad \lambda_{min} \leq \lambda \leq \lambda_{max}$$

$$0 \leq A(r) \leq \frac{4}{\pi} \arcsin\left(\frac{R_{solid}}{r} \sin\left(\frac{\pi}{4}\right)\right) \qquad R_{solid} < r \leq R \qquad \text{Model 1}$$

$$0 \leq A(r) \leq \frac{4}{\pi} \arcsin\left(\frac{2R_{solid}}{r} \sin\left(\frac{\pi}{4}\right)\right) \qquad 2R_{solid} < r \leq R \qquad \text{Model 2}$$

It can be seen that there are a few differences between this optimization problem and Vanderbei's optimization problem.[11] First, this study treats the contrast level as the objective variable. Because the occulter is small, it is hoped that monolithic petals can be machined from an appropriate material. Thus, there is no benefit to smoothing the apodization function beyond what is required for manufacturing. The manufacturing constraint is simply enforced by placing a hard limit on the second derivative of the apodization function. The second key difference is that the shadow contrast requirement is enforced for all separations within 1% of the baseline. This is required to ensure that the optical performance is sufficient if the science phase GN&C system only counteracts differential acceleration perpendicular to the line-of-sight. The final difference is that this problem includes geometric constraints associated with the presented engineering models.

Now that the optimization problem is formulated, it is possible to address the pareto-optimal performance characterization. Using the described optimization problem, an optimal occulter geometry is computed for each engineering model for each combination of critical design variables in the design envelope described in Table 2 with a few exceptions. First we ignore designs with Fresnel numbers less than two because these geometries will not have sufficient phase complexity to produce a deep shadow. We also ignore designs in which the shadow radius is larger than the occulter radius. Finally, we ignore designs that include wavelengths of less than 150 nm in the science spectrum because such spectra are impractical given the constraints of small telescopes. Subject to these constraints, there are 15,280 feasible combinations of design variables for each engineering model. The optimization problem is solved using CVX, a Matlab package for specifying and solving convex programs.[21,22] Because each of the optimization problems are independent, multiple programs are solved simultaneously on a supercomputer.

6. RESULTS

The results of this study suggest that there exist a wide range of occulter geometries capable of achieving the required contrast performance to image exozodiacal dust disks. The satisfactory design envelope is much larger for Model 2 than for Model 1, largely due to the constraint associated with folding the petals onto the sides of the spacecraft bus. For example, the geometries proposed by previous authors[5,11] are qualitatively similar and characterized by a slow, smooth separation of the petals. This geometry is incompatible with the previously described folding constraint for Model 1. To illustrate this difference, Figure 8 illustrates the difference between the geometries produced with the Model 1 and Model 2 geometric constraints for a specific design point. The green area in the figure denotes the area of the occulter plane that the panels are allowed to occupy due to their engineering constraints. It can be seen that the Model 2 occulter closely resembles the geometries published by previous authors, while the Model 1 occulter exhibits very long, slender petals to accomodate the folding constraint. The drastic difference in geometry results in reduced contrast performance for the Model 1 occulter. While the Model 2 occulter has a contrast of better than 10^{-8}, the Model 1 occulter only has a contrast of 10^{-3}.

To illustrate how the occulter performance varies with the occulter radius and baseline separation, consider Figure 9, which illustrates the best contrast performance as a function of occulter radius and inter-spacecraft separation for a 20 cm radius shadow and a science instrument spectrum of 175-275 nm for both engineering models. In the figure, the diagonal lines are lines of constant IWA and the colored region is a contour plot of achievable contrast. The first conclusion that can be drawn from Figure 9 is that the achievable contrast varies roughly with the Fresnel number (see Appendix A for plots of Fresnel number against occulter radius and separation). Indeed, Model 2 occulters can achieve sufficient contrast for exozodii imaging with Fresnel numbers as low as 6. Thus, for Model 2 geometries, the path length from the telescope to the center and edge of the occulter need only vary by three wavelengths in order to achieve sufficient contrast for direct imaging of exozodii. The second conclusion is that only a few Model 1 occulter geometries using this science spectrum are able to achieve 10^{-6} contrast. These geometries also require an IWA of 800 mas or larger. On the other hand, Model 2 occulters have a large envelope in which contrast of 10^{-6} is achievable. Furthermore, these occulters can achieve

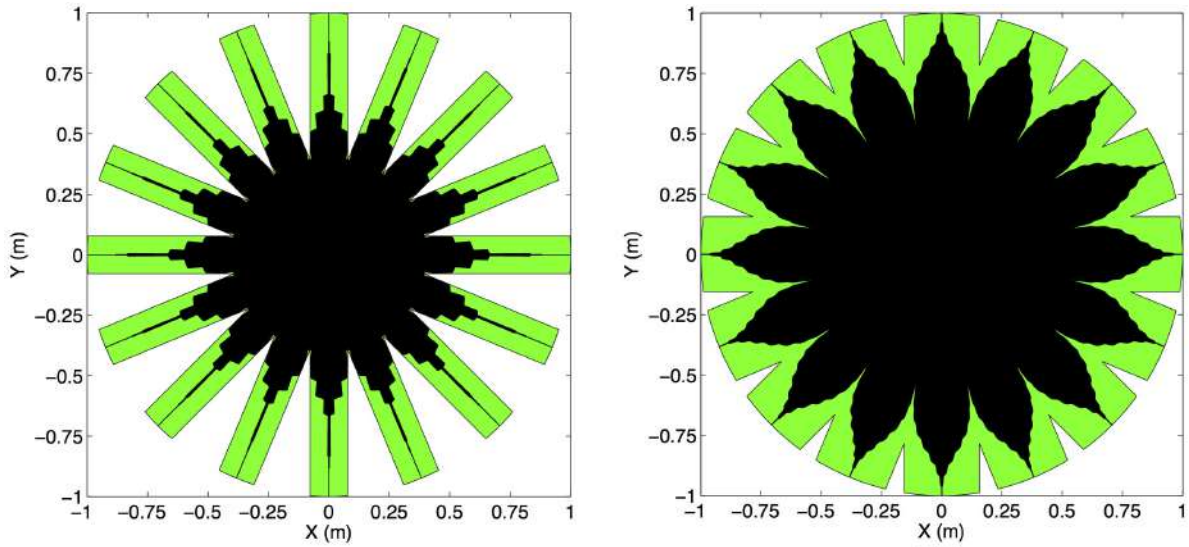

Figure 8. Comparison of geometries from constraints required by Model 1 (left) and Model 2 (right)

sufficient contrast for exozodiacal dust imaging with inner working angles of less than 400 mas. Data slices for other science spectra for Model 1 and Model 2 occulters are included in Appendices B and C, respectively. In these plots, occulter contrast values better than 10^{-10} are neglected in the interest of clarity. It will later be demonstrated that these contrast levels would be very difficult to realize on a miniaturized occulter due to manufacturing precision requirements. One key conclusion that can be drawn from the plots in Appendices B and C is that the achievable contrast is relatively insensitive to the width of the bandwidth as long as the maximum wavelength is unchanged. The bandwidth is strongly correlated with the flux from the target to the science instrument, and should be maximized as much as possible in order to minimize the required integration time.

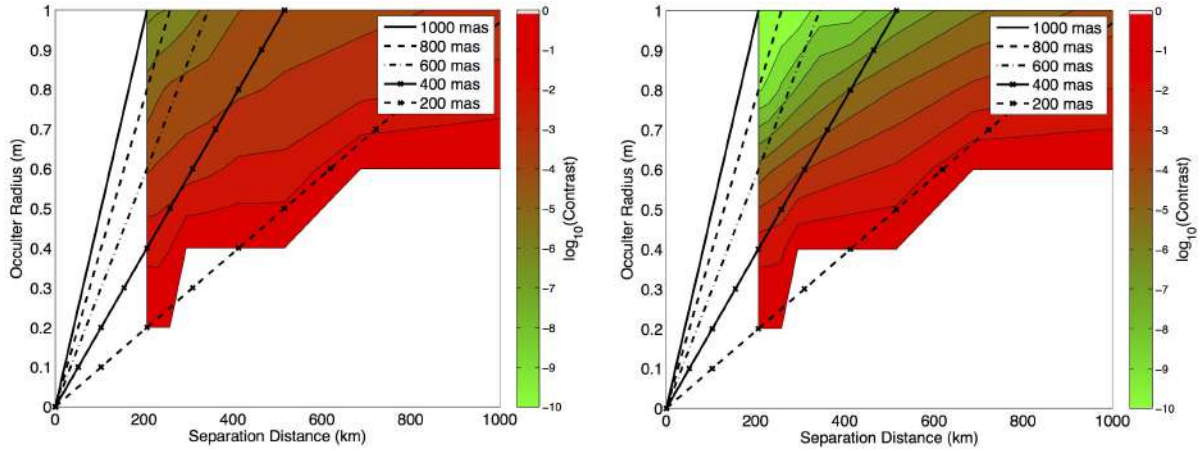

Figure 9. Optimal occulter contrast vs occulter radius and inter-spacecraft separation for a 175-275 nm science spectrum for Model 1 (left) and Model 2 (right) occulters with a 20 cm radius shadow

Because the Model 2 occulters exhibit the ability to achieve contrast levels beyond what is required for exozodiacal dust imaging, it is possible to design an occulter that produces less contrast, but with a larger shadow. As the achievable precision of the GN&C system used to keep the formation in alignment during the science phase is not yet known, this capability provides a valuable degree of design flexibility. To illustrate this behavior, consider Figure 10. This figure illustrates the largest shadow radius for which the occulter can achieve

10^{-6} contrast for a 175-275 nm science spectrum. As with the contrast plots, the maximum shadow radius tends to increase with the Fresnel number. It can be seen that in order to achieve an IWA of 500 mas or less in this case, the shadow radius will be no larger than 0.2 m, requiring a very precise GN&C system. However, if the IWA requirement is relaxed, occulter geometries can be designed that allow for shadow radii as large as 0.4 m. Additional plots of the maximum shadow radius consistent with a 10^{-6} contrast requirement for Model 2 occulters are included in Appendix D. Plots for Model 1 occulters are not included because these geometries lack the required excess suppression to allow larger shadows.

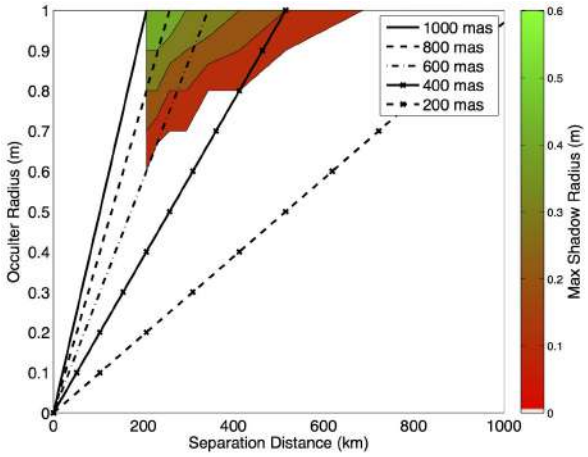

Figure 10. Maximum shadow radius for 10^{-6} contrast for Model 2 occulters with a 175-275 nm science spectrum

In summary, there exist a wide range of occulters that satisfy the optical requirements for imaging exozodiacal dust disks. The achievable contrast of a miniaturized occulter depends primarily on the enforced geometric constraints, the Fresnel number, and the size of the required shadow. Although having petals that can be deployed from the sides of the spacecraft bus is attractive due to its simplicity, occulters designed for this purpose exhibit diminished contrast performance. However, allowing for secondary winglets to be deployed from these petals allows occulter geometries very similar to those published by previous authors, which exhibit high contrast. Additionally, in agreement with previous authors the performance of these occulters varies with the Fresnel number. However, we have identified occulter geometries with sufficient contrast to image exozodiacal dust with Fresnel numbers as low as 6, which is significantly lower than values discussed in literature.[5] This is due to the fact that imaging exozodiacal dust requires lower contrast than imaging exoplanets. Finally, the occulter contrast depends strongly on the required shadow radius because the occulter radius is constrained to be no larger than 1 m. For the purpose of exozodiacal dust imaging, these occulters can achieve 10^{-6} contrast with shadow radii as large as 0.4 m, though this depends on the target IWA. Thus, there exists a substantial trade space between IWA, required contrast, shadow size, and science spectra that can be explored for a specified target.

7. MANUFACTURING CONSIDERATIONS

The previous section demonstrated that occulter geometries with scientifically relevant contrast performance exist. It is now necessary to verify that manufacturing considerations to not severely compromise the performance of these designs. There are two primary considerations that determine whether an occulter is realizable: 1) the required number of petals, and 2) the required precision of the manufacturing process of the optical edge of the occulter. For preliminary analysis purposes, we analyze these considerations in the context of a promising design from the previously described data set. The properties of the chosen design are given in Table 3. This occulter geometry is illustrated in Figure 8 (right). This occulter has a nominal contrast of 3×10^{-9}. For simplicity, both number of petals and manufacturing tolerances are addressed using this geometry.

Table 3. Example occulter design for manufacturing analysis

R (m)	z (km)	ρ (m)	λ_{max}(nm)	Bandwidth (nm)	R_{solid}/R
1.0	412	0.2	275	100	0.4

7.1 Adding Petals

In the same manner as described by previous authors,[11] the design of the occulter has thus far assumed that the shadow profile is axially symmetric. However, including a finite number of petals introduces a periodic oscillations about the axis of the shadow. It is therefore necessary to determine how many petals are necessary to ensure that these oscillations do no impact the contrast performance. Consider Equation (8), which includes the effect of a finite number of petals, which is assumed to be even. It can be seen that the perturbation due to petals is maximized when $\phi = 0$. To assess the number of petals, the electric field in the aperture plane along a line defined by $\phi = 0$ using the example occulter is computed for numbers of petals ranging from 4 to 32 using the first six terms of the Jacobi-Anger expansion. The contrast provided by the occulter is plotted against the number of petals in Figure 11. In agreement with previous authors, the number of petals will need to be at

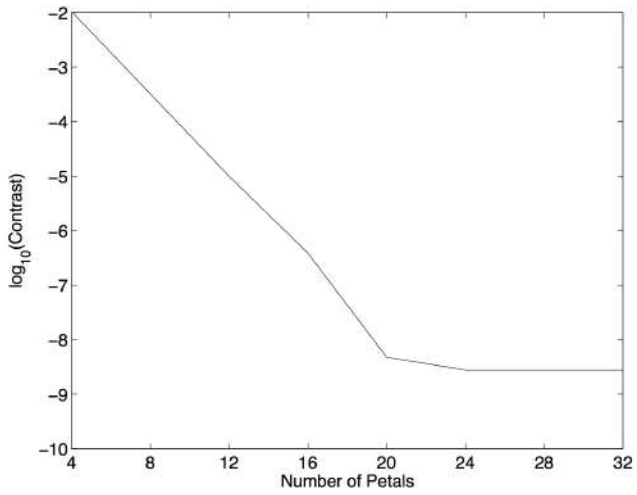

Figure 11. Occulter contrast vs number of petals

least 16 in order for the occulter to be scientifically relevant. Increasing the number of petals beyond 20 would not improve performance of this geometry. Considering the requirements of the presented engineering models in Sec. 4, this requirement would require a spacecraft bus with a large number of sides to accommodate a Model 1 occulter. However, deployment of a Model 2 occulter with 16 or more petals on a cubic spacecraft bus would only require a modification of the shape of the winglet illustrated in Figure 7 to include a larger portion of the petal.

7.2 Manufacturing Tolerances

It is now necessary to asses whether the example occulter, when manufactured with current technologies, will maintain scientifically relevant contrast performance. To accomplish this, we introduce a simplified subset of the design perturbations introduced by Shaklan[23,24] to assess large-scale occulters. The modeled perturbations include a flat error in the apodization function and a set of sine waves of varying frequencies over the petal. The performance of occulters subject to manufacturing errors is computed by calculating the electric field in the aperture plane from the perturbed apodization function, $A^*(r)$, which is given by

$$A^*(r) = A(r) + \delta A\, e(r), \tag{10}$$

where $\delta A(r)$ denotes the magnitude of the perturbation and $e(r)$ denotes the perturbation profile in the range $R_s \leq r \leq R$. The sine wave error profiles are given by

$$e(r) = \sin\Big(\frac{2\pi k}{R - R_{solid}}(r - R_{solid})\Big), \tag{11}$$

where k is the integer number of cycles per petal. The achievable occulter contrast is plotted against the amplitude of each of the described perturbations in Figure 12. The figure demonstrates that the contrast performance is most sensitive to a sine wave profile of 4 cycles per petal. This is expected because the Fresnel number of the example geometry is approximately 8, so the perturbation profile is in phase with the light diffracting between the petals. It can be seen that the occulter can tolerate errors in the apodization function as large as 100 parts per million (ppm) before the contrast performance degrades beyond 10^{-6}. If we assume that the occulter has 16 petals, then this corresponds to a displacement of the optical edge of approximately 20 microns on each petal. It follows that the manufacturing precision required to manufacture a small-scale occulter capable of achieving 10^{-6} contrast is comparable to the precision required to manufacture a large-scale occulter for exoplanet imaging.[23] However, manufacturing a small occulter with this precision should be a simpler task than manufacturing a large-scale occulter.

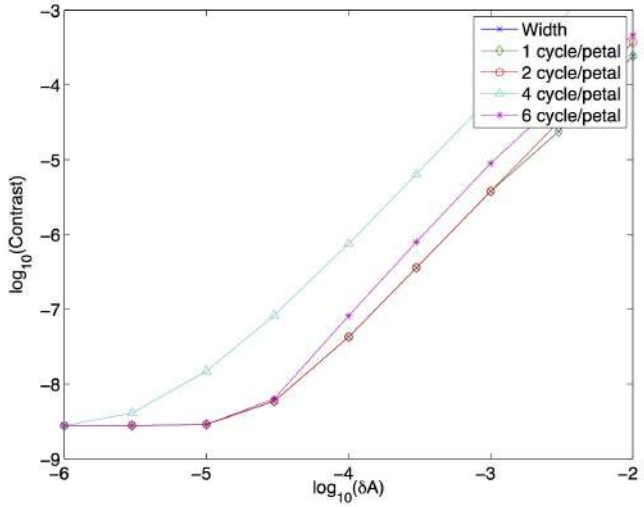

Figure 12. Occulter contrast vs apodization perturbation magnitude

To understand why the manufacturing tolerances on small occulters are comparable to those of large occulters, consider the effect of a hole in the center of the occulter (e.g. due to a micrometeoroid). As described by Shaklan,[23] the normalized flux, I/I_0 in the telescope aperture plane from a hole of area A_h in the center of the occulter is given by

$$\frac{I}{I_0} = \frac{A_h^2}{\lambda^2 z^2}. \tag{12}$$

The normalized flux depends only on the area of the hole, the inter-spacecraft separation, and the wavelength. For the proposed mission concept, the minimum wavelength is reduced by a factor of two compared to large-scale occulters and the inter-spacecraft separation is reduced by at least a factor of ten. It is clear that in order to maintain similar contrast, small-scale occulters would only be able to tolerate very small holes. However, because the proposed concept aims primarily to image exozodiacal dust disks at lower contrast levels, the manufacturing tolerances are nearly unchanged.

8. CONCLUSIONS

In this work we endeavored to characterize the relationship between the contrast performance of miniaturized occulters compatible with micro- or nano-satellites deployed in earth orbit in the context of a mission concept

proposed by the authors. The proposed mission concept would demonstrate the validity of the distributed occulter/telescope mission concept and collect images of exozodiacal dust disks at only a fraction of the cost of a full-scale mission. This work includes several contributions to the state-of-the-art. First, it includes a design envelope for occulters compatible with micro- or nano-satellites in earth orbit derived from simple considerations in including geometric requirements of diffractive optics, mission operations considerations, and manufacturing considerations. Second, this work demonstrates that there exist a wide variety of occulter geometries capable of achieving sufficient contrast to image exozodiacal dust disks in the ultraviolet spectrum. Indeed, some geometries provide sufficient contrast to image exoplanets. However, manufacturing considerations suggest that achieving such a high contrast level in practice at such a small size would be challenging. Finally, a preliminary tolerance analysis suggests that manufacturing a small occulter to image exozodiacal dust would be no more challenging than manufacturing a large occulter for exoplanet imaging. These results, in conjunction with a concurrent formation design study by the authors, suggest that deploying a miniaturized technology demonstrator in earth orbit could simultaneously validate key aspects of the distributed occulter/telescope mission concept and collect images of exozodii.

APPENDIX A. FRESNEL NUMBER PLOTS

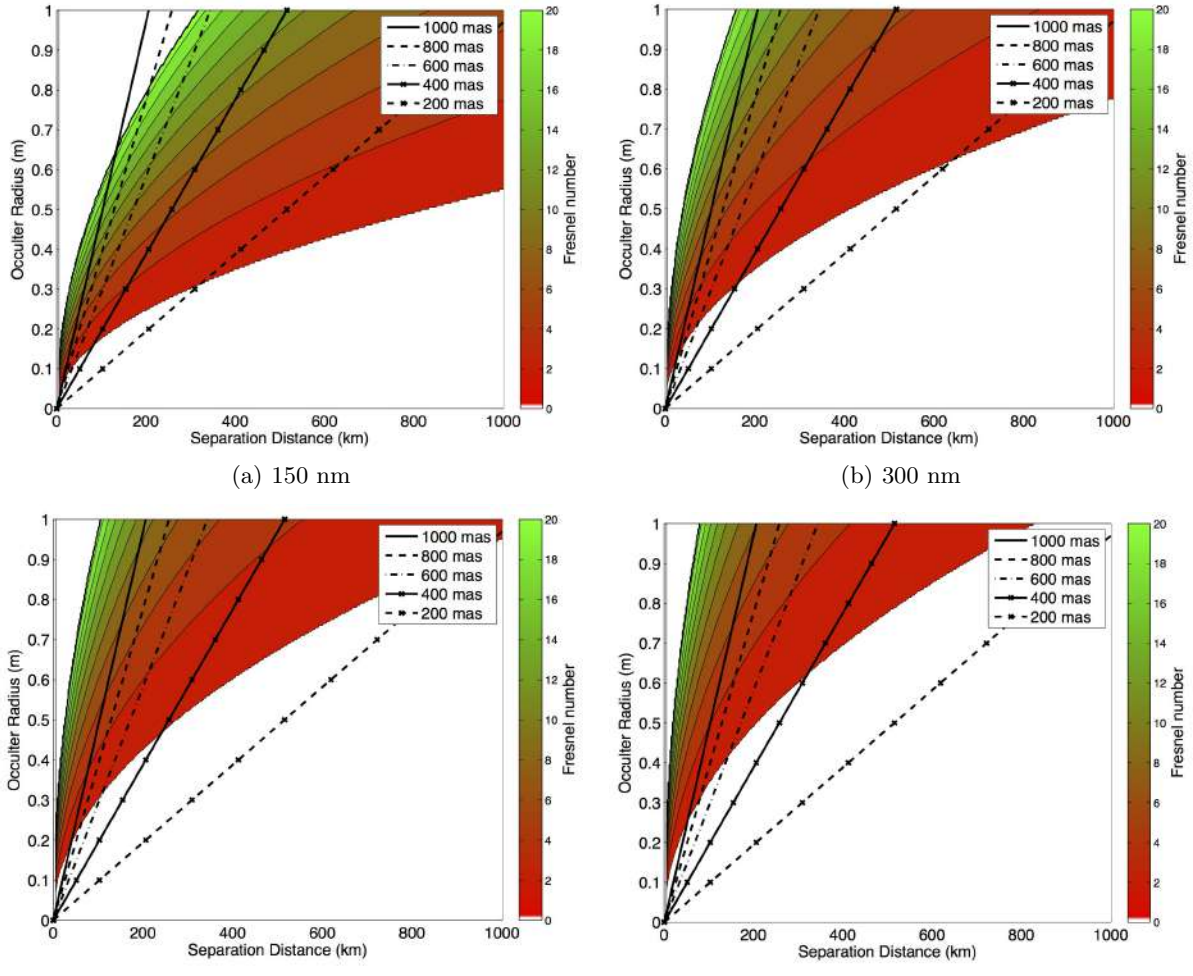

(a) 150 nm

(b) 300 nm

(c) 450 nm

(d) 600 nm

Figure 13. Plots of the relationships between occulter radius, inter-spacecraft separation, inner working angle, and the Fresnel number

APPENDIX B. MODEL 1 CONTRAST DATA SLICES

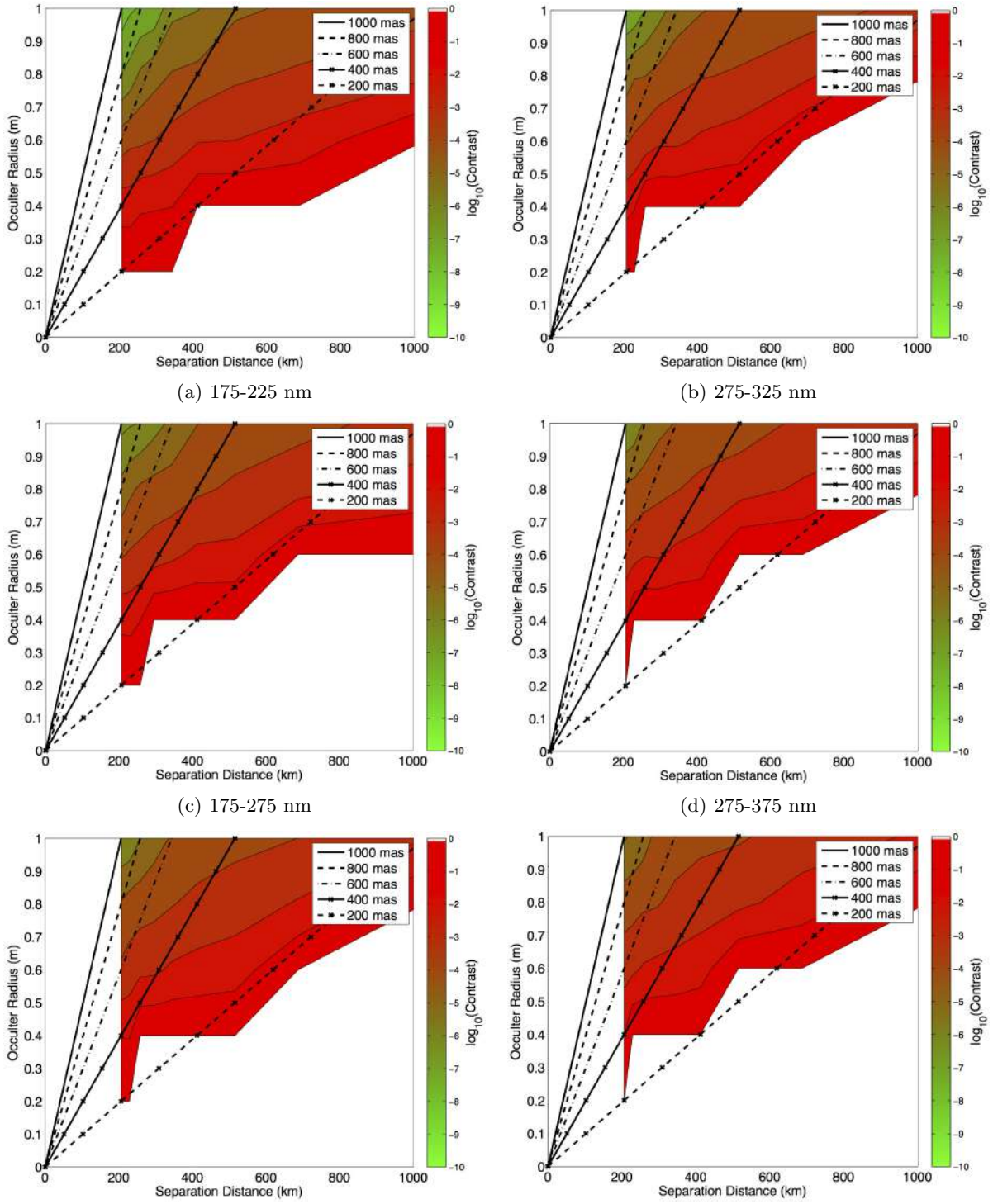

(a) 175-225 nm

(b) 275-325 nm

(c) 175-275 nm

(d) 275-375 nm

(e) 175-325 nm

(f) 175-375 nm

Figure 14. Model 1 data slices of optimal contrast values plotted against occulter radius and inter-spacecraft separation for specified science spectra for a 20 cm radius shadow

APPENDIX C. MODEL 2 CONTRAST DATA SLICES

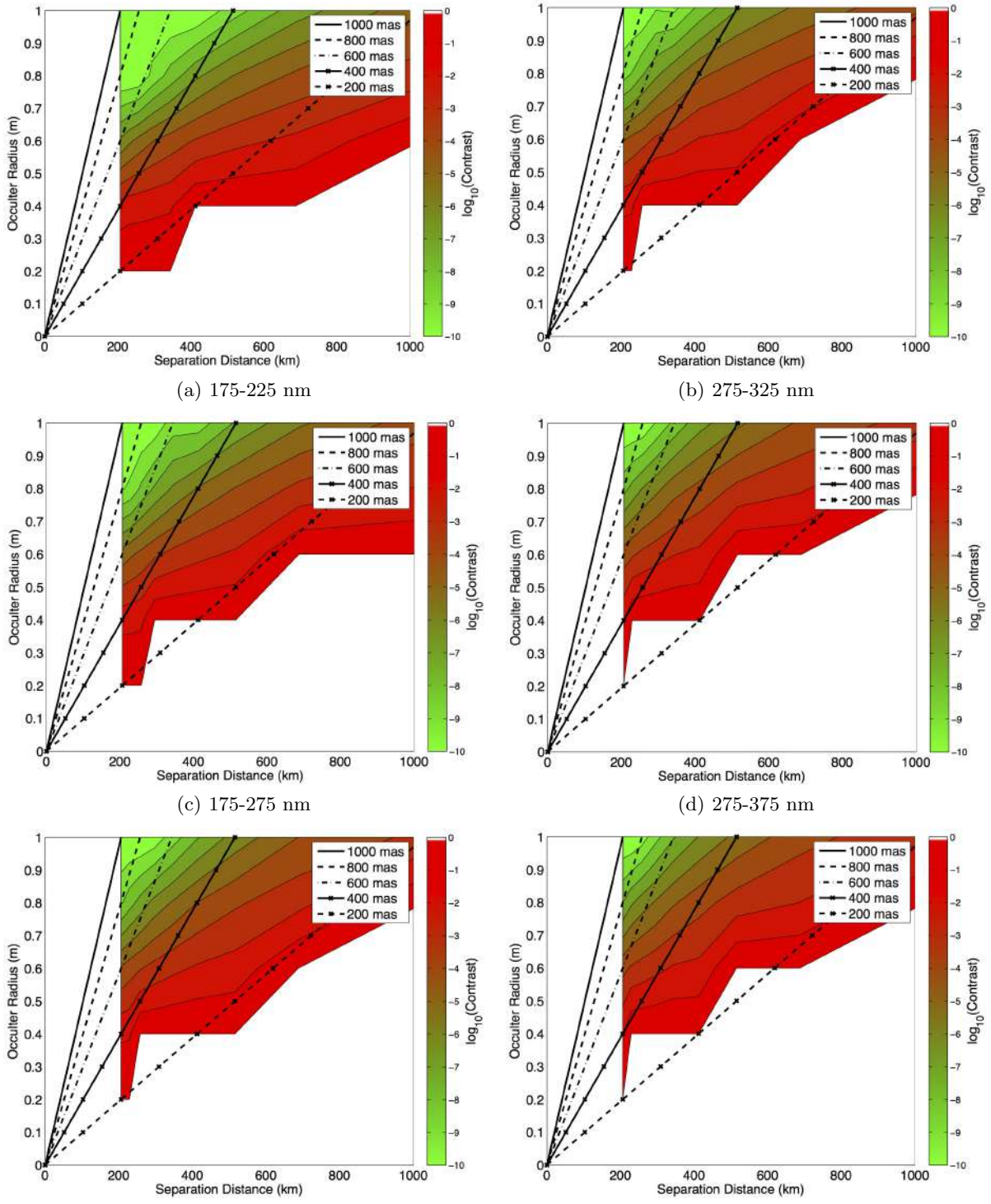

(a) 175-225 nm

(b) 275-325 nm

(c) 175-275 nm

(d) 275-375 nm

(e) 175-325 nm

(f) 175-375 nm

Figure 15. Model 2 data slices of optimal contrast values plotted against occulter radius and inter-spacecraft separation for specified science spectra for a 20 cm radius shadow

APPENDIX D. MODEL 2 SHADOW RADIUS DATA SLICES

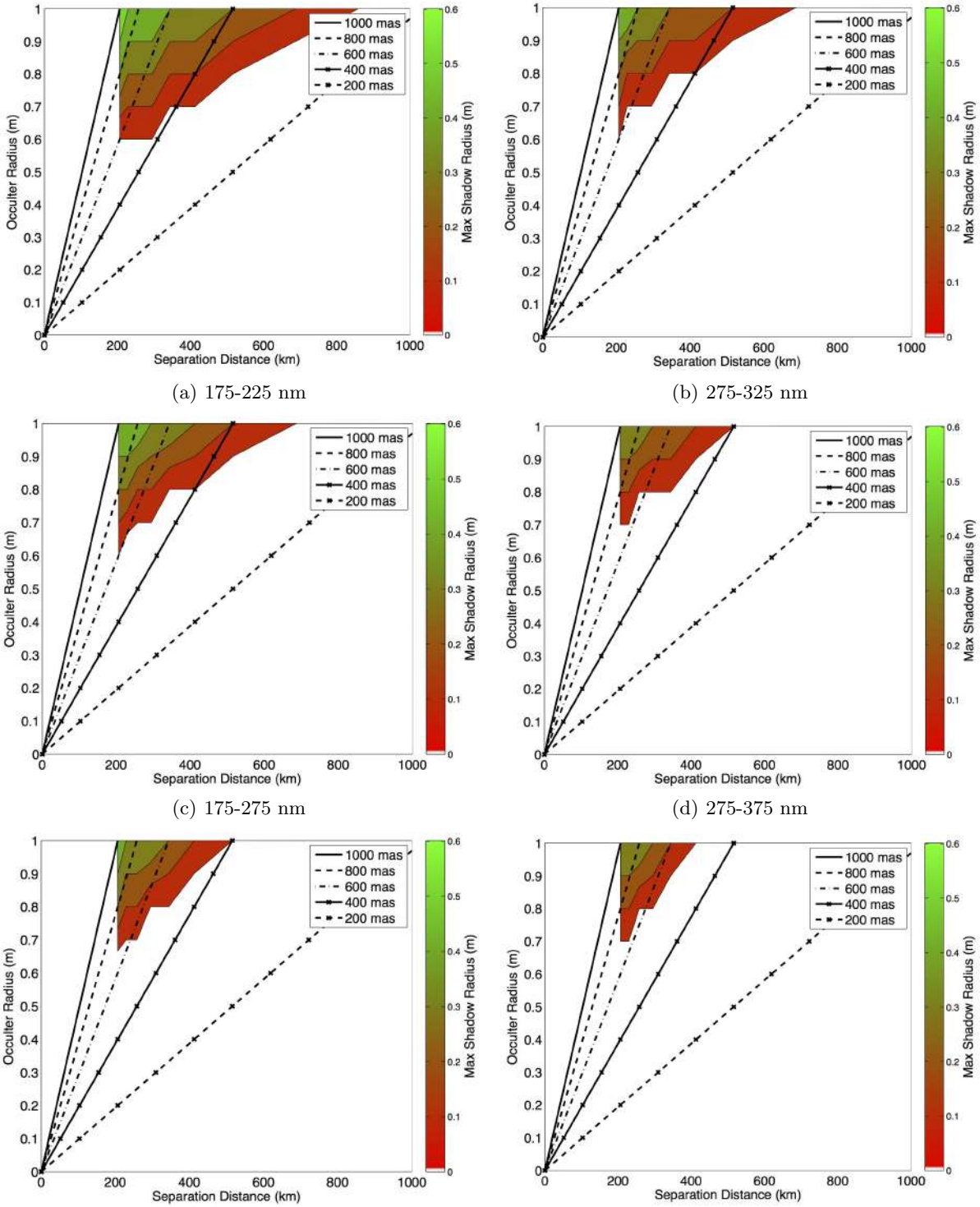

(a) 175-225 nm

(b) 275-325 nm

(c) 175-275 nm

(d) 275-375 nm

(e) 175-325 nm

(f) 175-375 nm

Figure 16. Model 2 maximum shadow radius for 10^{-6} contrast for specified science spectra

REFERENCES

[1] Borucki, W. J., Koch, D., Basri, G., Batalha, N., Brown, T., Caldwell, D., Caldwell, J., Christensen-Dalsgaard, J., Cochran, W. D., DeVore, E., et al., "Kepler planet-detection mission: introduction and first results," *Science* **327**(5968), 977–980 (2010).

[2] Marois, C., Macintosh, B., Barman, T., Zuckerman, B., Song, I., Patience, J., Lafrenière, D., and Doyon, R., "Direct imaging of multiple planets orbiting the star HR 8799," *Science* **322**(5906), 1348–1352 (2008).

[3] Stapelfeldt, K. R., Brenner, M. P., Warfield, K. R., Dekens, F. G., Belikov, R., Brugarolas, P. B., Bryden, G., Cahoy, K. L., Chakrabarti, S., Dubovitsky, S., et al., "Exo-C: a probe-scale space mission to directly image and spectroscopically characterize exoplanetary systems using an internal coronagraph," in [*SPIE Astronomical Telescopes and Instrumentation*], 91432K–91432K, International Society for Optics and Photonics (2014).

[4] Spergel, D., Gehrels, N., Breckinridge, J., Donahue, M., Dressler, A., Gaudi, B. S., Greene, T., Guyon, O., Hirata, C., Kalirai, J., et al., "Wide-field infrared survey telescope-astrophysics focused telescope assets WFIRST-AFTA final report," (2013).

[5] Cash, W., "Detection of Earth-like planets around nearby stars using a petal-shaped occulter," *Nature* **442**(7098), 51–53 (2006).

[6] D'Amico, S., Ardaens, J.-S., and Larsson, R., "Spaceborne autonomous formation-flying experiment on the PRISMA mission," *Journal of Guidance, Control, and Dynamics* **35**(3), 834–850 (2012).

[7] Landgraf, M. and Mestreau-Garreau, A., "Formation flying and mission design for Proba-3," *Acta Astronautica* **82**(1), 137–145 (2013).

[8] Roscoe, C. W. T., Vadali, S. R., Alfriend, K. T., and Desai, U. P., "Optimal formation design for magnetospheric multiscale mission using differential orbital elements," *Journal of Guidance, Control, and Dynamics* **34**(4), 1070–1080 (2011).

[9] Seager, S., Cash, W. C., Kasdin, N. J., Sparks, W. B., Turnbull, M. C., Kuchner, M. J., Roberge, A., Domagal-Goldman, S., Shaklan, S., Thomson, M., et al., "Exo-S: A Probe-scale Space Mission to Directly Image and Spectroscopically Characterize Exoplanetary Systems Using a Starshade and Telescope System," in [*American Astronomical Society Meeting Abstracts*], **224** (2014).

[10] Kolmas, J., Banazadeh, P., Koenig, A. W., and D'Amico, S., "Preliminary System Design of a Miniaturized Distributed Occulter/Telescope for Direct Imaging of Exozodiacal Dust and Exoplanets," in [*Proceedings of the 7th European CubeSat Symposium*], (2015). (Accepted).

[11] Vanderbei, R. J., Cady, E., and Kasdin, N. J., "Optimal occulter design for finding extrasolar planets," *The Astrophysical Journal* **665**(1), 794 (2007).

[12] Glassman, T., Lo, A. S., Arenberg, J., Cash, W., and Noecker, C., "Starshade scaling relations," in [*SPIE Optical Engineering + Applications*], 744013–744013, International Society for Optics and Photonics (2009).

[13] Cady, E., "Nondimensional representations for occulter design and performance evaluation," in [*SPIE Optical Engineering + Applications*], 815112–815112, International Society for Optics and Photonics (2011).

[14] Cumming, A., Butler, R. P., Marcy, G. W., Vogt, S. S., Wright, J. T., and Fischer, D. A., "The keck planet search: detectability and the minimum mass and orbital period distribution of extrasolar planets," *Publications of the Astronomical Society of the Pacific* **120**(867), 531–554 (2008).

[15] Hatzes, A. P., Cochran, W. D., McArthur, B., Baliunas, S. L., Walker, G. A. H., Campbell, B., Irwin, A. W., Yang, S., Kürster, M., Endl, M., et al., "Evidence for a long-period planet orbiting eridani," *The Astrophysical Journal Letters* **544**(2), L145 (2000).

[16] Graham, J. R., Kalas, P. G., and Matthews, B. C., "The Signature of Primordial Grain Growth in the Polarized Light of the AU Microscopii Debris Disk," *The Astrophysical Journal* **654**(1), 595 (2007).

[17] Board, S. S. et al., [*Panel Reports–New Worlds, New Horizons in Astronomy and Astrophysics*], National Academies Press (2011).

[18] Koenig, A. W., D'Amico, S., Macintosh, B., and Titus, C. J., "Optimal Formation Design of a Miniaturized Distributed Occulter/Telescope in Earth Orbit," in [*Proceedings of the AIAA/AAS Astrodynamics Specialist Conference*], (2015).

[19] Peters, T. V., Branco, J., Escorial, D., Castellani, L. T., and Cropp, A., "Mission analysis for PROBA-3 nominal operations," *Acta Astronautica* **102**, 296–310 (2014).

[20] Goodman, J., "Introduction to Fourier Optics," (2008).

[21] Grant, M. and Boyd, S., "CVX: Matlab Software for Disciplined Convex Programming, version 2.1." URL: http://cvxr.com/cvx (Mar. 2014).

[22] Grant, M. and Boyd, S., "Graph implementations for nonsmooth convex programs," in [*Recent Advances in Learning and Control*], *Lecture Notes in Control and Information Sciences*, 95–110, Springer-Verlag Limited (2008). URL: http://stanford.edu/ boyd/graph_dcp.html.

[23] Shaklan, S. B., Noecker, M. C., Glassman, T., Lo, A. S., Dumont, P. J., Kasdin, N. J., Cady, E. J., Vanderbei, R., and Lawson, P. R., "Error budgeting and tolerancing of starshades for exoplanet detection," in [*SPIE Astronomical Telescopes + Instrumentation*], 77312G–77312G, International Society for Optics and Photonics (2010).

[24] Shaklan, S. B., Marchen, L., Lisman, P. D., Cady, E., Martin, S., Thomson, M., Dumont, P., and Kasdin, N. J., "A starshade petal error budget for exo-earth detection and characterization," in [*SPIE Optical Engineering + Applications*], 815113–815113, International Society for Optics and Photonics (2011).